Interfacial Electron Transfer of Ni$_2$P–NiP$_2$ Polymorphs Inducing Enhanced Electrochemical Properties

Tong Liu, Anran Li, Chengbo Wang, Wei Zhou,* Shijie Liu, and Lin Guo

Heterointerface engineering can be used to develop excellent catalysts through electronic coupling effects between different components or phases. As one kind of promising Pt-free electrocatalysts for hydrogen evolution reaction (HER), pure-phased metal phosphide exhibits the unfavorable factor of strong or weak H*-adsorption performance. Here, 6 nm wall-thick Ni$_2$P–NiP$_2$ hollow nanoparticle polymorphs combining metallic Ni$_2$P and metalloid NiP$_2$ with observable heterointerfaces are synthesized. It shows excellent catalytic performance toward the HER, requiring an overpotential of 59.7 mV to achieve 10 mA cm^{-2} with a Tafel slope of 58.8 mV dec^{-1}. Density functional theory calculations verify electrons' transfer from P to Ni at the heterointerfaces, which decreases the absolute value of H* adsorption energy and simultaneously enhance electronic conductivity. That is, the heterojunctions balance the metallic Ni$_2$P and the metalloid NiP$_2$ to form an optimized phosphide polymorph catalyst for the HER. Furthermore, this polymorph combination is used with NiFe-LDH nanosheets to form an alkaline electrolyzer. It shows highly desirable electrochemical properties, which can reach 10 mA cm^{-2} in 1 M KOH at 1.48 V and be driven by an AAA battery with a nominal voltage of 1.5 V. The work about interfacial charge transfer might provide an insight into designing excellent polymorph catalysts.

Along with the development of hydrogen technologies including hydrogen vehicles and hydrogen generator, electrocatalytic water splitting has been regard as a sustainable approach for large-scale hydrogen production.[1,2] Water electrolysis consists of two half reactions, the hydrogen evolution reaction (HER) and the oxygen evolution reaction (OER). It usually requires over 1.8 V to overcome the reaction energy barrier mainly caused by complex electron redox process of both reactions.[3] It is thus crucial to develop highly efficient catalysts to reduce overpotential to save energy.

T. Liu, Dr. A. Li, Prof. W. Zhou, S. Liu, Prof. L. Guo
School of Chemistry
Beijing Advanced Innovation Center for Biomedical Engineering
Beihang University
Beijing 100191, China
E-mail: zhouwei@buaa.edu.cn
C. Wang
College of Chemistry and Molecular Engineering
Peking University
Beijing 100871, China

The ORCID identification number(s) for the author(s) of this article can be found under https://doi.org/10.1002/adma.201803590.

Recently, metal phosphides as HER electrocatalysts have been confirmed to be promising Pt replacement candidates, owing to their low cost and high reactivity.[4–9] As is known, transition-metal phosphides have many chemical formulas with compositions from metal-rich M$_4$P to phosphorus-rich MP$_{15}$. For example, nickel forms eight phosphides, including Ni$_3$P, Ni$_5$P$_2$, Ni$_{12}$P$_5$, Ni$_2$P, Ni$_5$P$_4$, NiP, NiP$_2$, and NiP$_3$. Due to the high electronic conductivity of metallic metal phosphides (the atomic ratio of M and P is greater than one),[10] and the high activity of metalloid metal phosphides (the atomic ratio of M and P is less than or equal to one),[11,12] these phosphides show different properties toward HER. According to some density functional theory (DFT) calculation results, the absolute values of Gibbs free energy of hydrogen adsorption (ΔG_{H*}) for pure-phase metal compounds are often far from to zero.[12–18] It is worth noting that the ΔG_{H*} can serve as a critical factor to evaluate the HER activities of electrocatalysts. A catalyst that gives $\Delta G_{H*} = 0$ is served as an ideal candidate for HER. The higher absolute values of ΔG_{H*} means a unpreferable H* adsorption.[19–22] To solve the problem, the interface engineering has been regarded as an efficient strategy to change the valence electron state of active sites for electrocatalysts, and thus optimize the ΔG_{H*}.[13–17,23] For example, Wang et al. prepared 3D flower-like CoP$_3$/Ni$_2$P heterostructure through phosphating CoNi-LDH to improve its HER performance. They confirmed a significant decrease of charge density at the CoP$_3$/Ni$_2$P (Co) sites could improve desorption of the produced hydrogen and avoid catalyst poisoning.[15] Zhu et al. also verified the importance of interfaces of the Co-Ni$_3$N heterojunction for HER, which showed strong electron redistribution from Co to Ni and benefits in hydrogen adsorption.[17]

Nanostructures with high specific surface area such as hollow or hierarchical structures are desirable for catalysis. Thereinto, hollow structures with well-defined cavities could improve their HER performances through boosting mass transport and shortening diffusion distance owing to the merits of low density, large specific surface and large void space.[24] Remarkably, smaller sizes with thinner walls would better present the intrinsic properties. Inspired by our previous work, it might be a good choice to refine the size and wall thickness using other nickel compounds as sacrificial nanotemplates through

**ADVANCED
SCIENCE NEWS**
www.advancedsciencenews.com

**ADVANCED
MATERIALS**
www.advmat.de

phosphorization by nanoscaled Kirkendall effect.[25] Herein, we designed and synthesized 6 nm thin-wall hollow $Ni_2P–NiP_2$ polymorph through phosphorization, using NiS_2 single-crystal octahedrons as precursor. This polymorph exihibited superior HER performance, requiring an overpotential of 59.7 mV to achieve 10 mA cm^{-2} with a Tafel slope of 58.8 mV dec^{-1}. DFT calculation was carried out to better understand heterointerface effect on enhanced HER activity. Furthermore, we used this polymorph combined with NiFe-LDH nanosheets to design a practical efficient water electrolyzers, which could reach 10 mA cm^{-2} in 1 M KOH at 1.48 V and be driven by an AAA battery with a nominal voltage of 1.5 V.

As illustrated in **Figure 1**a, the hollow nickel phosphide polymorph was prepared by a solid-state phosphorization reaction between NaH_2PO_2 and the precursor of NiS_2 single-crystal octahedrons (Figure S1, Supporting Information) at 350 °C in N_2 atmosphere for 10 h through nanoscaled Kirkendall effect (details are given in the Experimental Section).[25,26] First, the precursor of NiS_2 single-crystal octahedrons reacts with PH_3
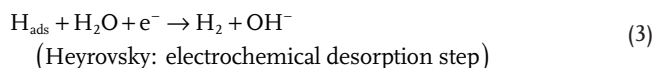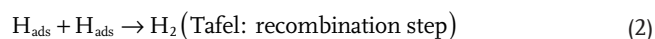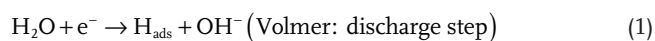
generated from the decomposition of NaH_2PO_2 in the solid-state phosphorization reaction on the surface. And then, followed by simultaneous diffusion of sulfur elements outward and diffusion of PH_3 into the NiS_2 octahedrons inward, nickel phosphide with hollow structure gradually formed. X-ray powder diffraction (XRD) pattern in Figure S2 (Supporting Information) shows the nickel phosphide has a good agreement with the component of Ni_2P (JCPDS NO. 03–0953) and NiP_2 (JCPDS NO. 21–0590). As shown in Figure 1b, the transmission electron microscopy (TEM) images show that the products are high-quality hollow nanoparticles with a similar size of ≈100 nm and an ultrathin wall thickness of ≈6 nm. The SAED pattern of a few $Ni_2P–NiP_2$ hollow nanoparticles (named as $Ni_2P–NiP_2$ HNPs) is shown in Figure 1c. The red polycrystalline rings displayed in the SAED can be indexed to the (211), (210), (201), and (111) planes of Ni_2P, while the blue ones can be indexed to the (311), (220), (221), (210), and (200) planes of NiP_2. The high-resolution TEM (HRTEM) image (Figure 1d) clearly shows the interface between the
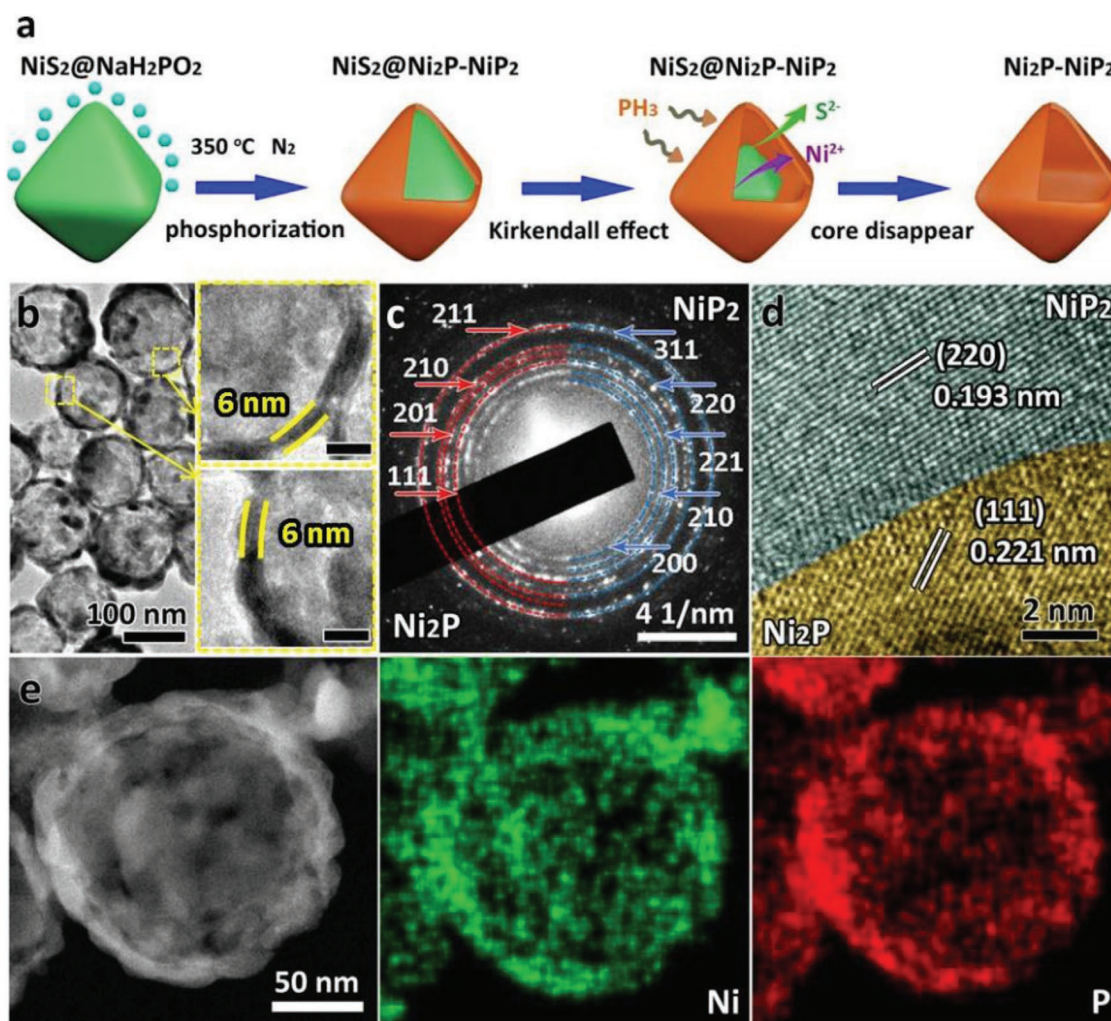
Figure 1. a) Schematic illustration for the formation of the $Ni_2P–NiP_2$ hollow nanoparticles ($Ni_2P–NiP_2$ HNPs). b) TEM images of the $Ni_2P–NiP_2$ HNPs with an average wall thickness of 6 nm (the scale bars in the right side of (b) are 20 nm). c) SAED pattern of the $Ni_2P–NiP_2$ HNPs with polycrystalline rings corresponding to Ni_2P (red rings) and NiP_2 (blue rings). d) HRTEM image of the $Ni_2P–NiP_2$ HNPs with clear interface between the (111) plane of Ni_2P and the (220) plane of NiP_2. e) STEM image of one hollow $Ni_2P–NiP_2$ nanoparticle and the related EDS mapping for elements of Ni and P.

ADVANCED
SCIENCE NEWS
www.advancedsciencenews.com

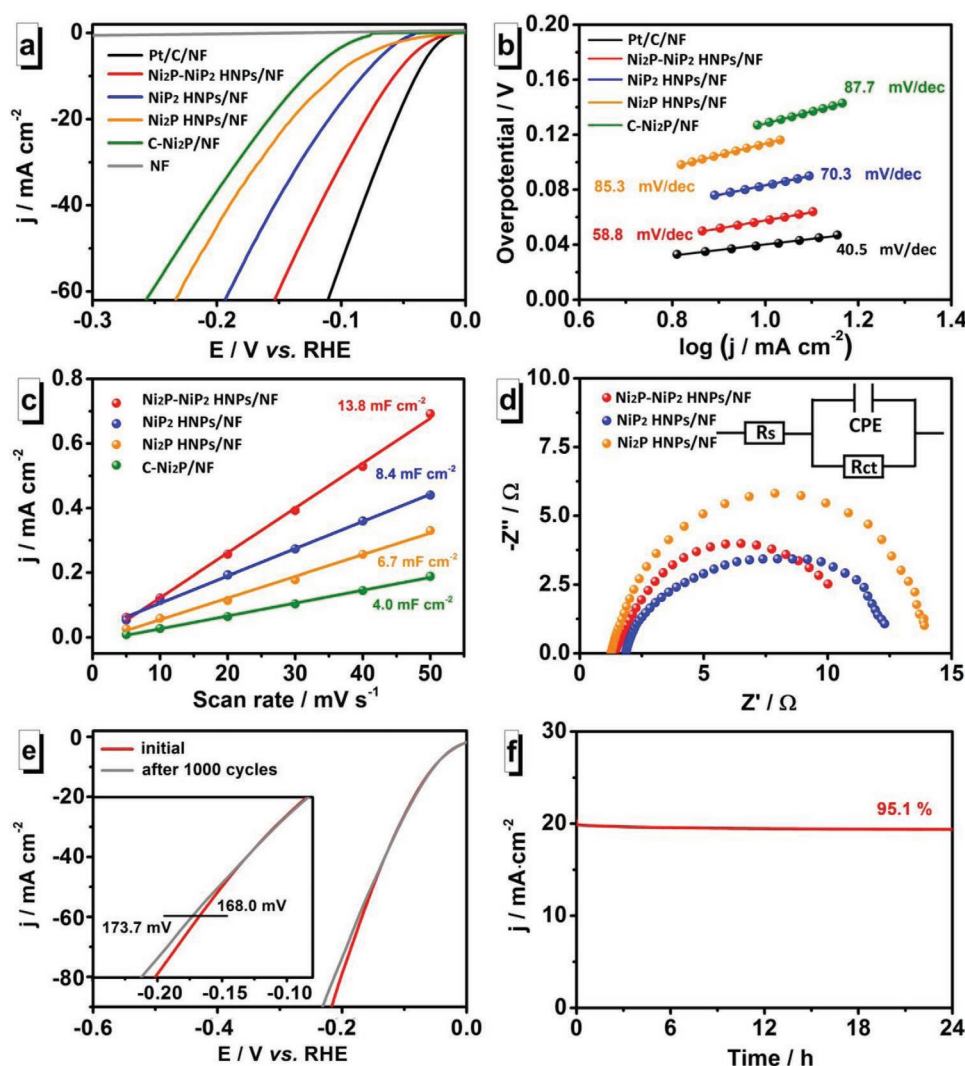ADVANCED
MATERIALS
www.advmat.de

(111) plane of Ni_2P and the (220) plane of NiP_2, corresponding to the lattice fringe spacings of 0.221 and 0.193 nm, respectively. Their corresponding FFT images (Figure S3, Supporting Information) also clearly show the cubic NiP_2 and hexagonal Ni_2P. These results agree well with the XRD result (Figure S2, Supporting Information). The mapping results in Figure 1e show homogeneous elemental distribution of Ni and P. The EDS result shows approximate atomic ratio of Ni:P = 0.46:0.54 (Figure S4, Supporting Information). We also used inductively coupled plasma optical emission spectrometer (ICP-OES) to fix the atomic ratio of Ni:P in the Ni_2P–NiP_2 HNPs to be 0.42:0.58. According to the two components of Ni_2P and NiP_2, their mole ratio was calculated to be 0.25:0.75. For comparison, we control reaction time and temperature and can obtain pure Ni_2P and close to pure NiP_2 hollow nanoparticles (named as Ni_2P HNPs and NiP_2 HNPs) with similar morphology as the Ni_2P–NiP_2 HNPs. The Ni_2P HNPs and NiP_2 HNPs were synthesized by a solid-state phosphorization reaction between NaH_2PO_2 and NiS_2 single-crystal octahedrons at 300 °C in N_2 atmosphere for 5 h and 400 °C in N_2 atmosphere for 10 h, respectively (details are given in the Experimental Section). Their corresponding characterizations are shown in Figures S5 and S6 (Supporting Information). It is clear that the phosphorization reaction tends to generate P-rich phase (NiP_2) at higher temperature, longer time and higher concentration of PH_3.

The electrocatalytic activity of the Ni_2P–NiP_2 HNPs for HER was tested in 1 M KOH solution using a typical three-electrode system. The sample was coated on cleaned Ni foam (NF, 1 cm × 1 cm) and used as work electrode after calcination at 350 °C under N_2 atmosphere to improve the adhesive force between catalysts and conductive substrates, and thus ensure the stability of HER activity. The commercial Pt/C, synthesized Ni_2P HNPs and NiP_2 HNPs, and commercial Ni_2P solid particles (named as C-Ni_2P, Figure S7, Supporting Information) were also coated on nickel foam for comparison. In **Figure 2**a, the Ni_2P–NiP_2 HNPs/NF only requires an overpotential of 59.7 mV to reach 10 mA cm^{-2}, which is comparable to the Pt/C/NF (41.5 mV), and much better than the Ni_2P HNPs/NF (104.8 mV), NiP_2 HNPs/NF (82.2 mV), and C-Ni_2P/NF (130.8 mV). This value is much lower than that of most reported phosphide electrocatalysts in 1 M KOH, such as $Ni_{0.51}Co_{0.49}P$ film (82 mV),[27] porous CoPO nanosheets (158 mV)[28] and 3D porous Ni/Ni_8P_3 (130 mV).[29] Even it is better than some hollow structured metal phosphides, such as CoP NPs/N doped carbon nanotube hollow polyhedron (115 mV),[5] Co_4NiP nanotubes (129 mV)[30] and multishelled Ni_2P (98 mV).[31] The overpotential details of recently reported nickel phosphides were also summarized in Table S1 (Supporting Information). Figure 2b shows the corresponding Tafel plots (η vs log (j)) about kinetic properties of HER. The hydrogen generation in base solution could be achieved by the Volmer–Tafel process or the Volmer–Heyrovsky pathway[32]

$$H_2O + e^- \rightarrow H_{ads} + OH^- \left(\text{Volmer: discharge step}\right) \quad (1)$$

$$H_{ads} + H_{ads} \rightarrow H_2 \left(\text{Tafel: recombination step}\right) \quad (2)$$

$$H_{ads} + H_2O + e^- \rightarrow H_2 + OH^- \quad (3)$$
$$\left(\text{Heyrovsky: electrochemical desorption step}\right)$$

Tafel slope values can be used to determine the HER pathway and the rate-limiting step for a catalyst. The Volmer, Tafel, and Heyrovsky reactions as the rate-limiting step involved in the HER could give a theoretical Tafel slope of 120, 30, and 40 mV dec^{-1}, respectively.[33] In our case, the Tafel slopes of the Ni_2P–NiP_2 HNPs/NF, Ni_2P HNPs/NF, NiP_2 HNPs/NF, C-Ni_2P/NF, and Pt/C/NF are 58.8, 85.3, 70.3, 87.7, and 40.5 mV dec^{-1}, respectively, showing these catalysts undergo Volmer reaction step and Heyrovsky reaction step in the HER. Notably, these results suggest the Ni_2P–NiP_2 HNPs/NF undergoes a much faster Volmer reaction than other nickel phosphide samples in the HER.[34] The exchange current densities (j_0) of the Ni_2P–NiP_2 HNPs/NF, Ni_2P HNPs/NF, NiP_2 HNPs/NF, C-Ni_2P/NF, and Pt/C/NF were separately calculated by extrapolating the Tafel plot to overpotential at 0 V, which represent the inherent HER activity of an electrocatalyst.[35] The exchange current density of the Ni_2P–NiP_2 HNPs/NF is 1.05 mA cm^{-2}, which is a little lower than that of Pt/C/NF (1.12 mA cm^{-2}) and larger than that of Ni_2P HNPs/NF (0.47 mA cm^{-2}), NiP_2 HNPs/NF (0.65 mA cm^{-2}), and C-Ni_2P/NF (0.35 mA cm^{-2}), revealing the Ni_2P–NiP_2 HNPs/NF possesses a higher HER activity compared to other nickel phosphide electrodes. Furthermore, we used the electrochemical double-layer capacitances (C_{dl}) to check the electrochemically active surface area (ECSA), and thus to evaluate the catalytic activity of catalysts.[8,36] The capacitance could be indirectly characterized by testing CV at different scanning rates from 5 to 50 mV s^{-1} in non-Faradaic region (Figure S8, Supporting Information). Figure 2c shows the plots of $\Delta j/2 = (j_{anodic} - j_{cathodic})/2$ at 0.21 V against scan rate. The fitting line slopes of the Ni_2P–NiP_2 HNPs/NF, Ni_2P HNPs/NF, NiP_2 HNPs/NF, and C-Ni_2P/NF are 13.8, 6.7, 8.4, and 4.0 mF cm^{-2}, respectively, which demonstrate hollow structure provides more effective active sites than commercial solid particles. Importantly, Ni_2P–NiP_2 HNPs/NF possesses more active sites and thus higher catalytic activity to its counterparts of the Ni_2P HNPs/NF and NiP_2 HNPs/NF.[13,15] To further study the HER kinetic, the electrochemical impedance spectroscopy (EIS) analysis was presented as the Nyquist plots (Figure 2d) fitted with the equivalent circuit (the inset). They disclose that the charge-transfer resistances (R_{ct}) of the Ni_2P–NiP_2 HNPs/NF, Ni_2P HNPs/NF, and NiP_2 HNPs/NF are 9.8, 13.2, and 11.1 Ω, respectively, suggesting a better charge transfer ability of the Ni_2P–NiP_2 HNPs/NF than the Ni_2P HNPs/NF and NiP_2 HNPs/NF.[13,15] The much improved conductivity might come from the heterointerface effect of Ni_2P–NiP_2 HNPs/NF.[13,15] As shown in Figure 2e, long-term cycling stability of the Ni_2P–NiP_2 HNPs/NF was checked by taking continuous cyclic voltammetry (CV) at an accelerated scanning rate of 50 mV s^{-1} till 1000 cycles. There is no obvious change in overpotential before 50 mA cm^{-2} and the overpotential at 60 mA cm^{-2} only increases 5.7 mV (173.7–168.0 mV). That is, the Ni_2P–NiP_2 HNPs/NF catalyst shows negligible catalytic degradation. The current density at an overpotential of 85 mV exhibits a 4.9% degradation even after 24 h in Figure 2f, also confirming its electrochemical stability. The compositional stability of Ni_2P–NiP_2 HNPs through HER process was investigated by X-ray photoelectron spectra (XPS) characterization. The high-resolution XPS spectra of Ni 2p and P 2p from Ni_2P–NiP_2 HNPs before and after 1000 linear sweep voltammetry (LSV) cycles are shown in

**ADVANCED
SCIENCE NEWS**

www.advancedsciencenews.com

**ADVANCED
MATERIALS**

www.advmat.de

Figure 2. a) HER polarization curves of the Ni_2P–NiP_2 HNPs/NF, Ni_2P HNPs/NF, NiP_2 HNPs/NF, C-Ni_2P/NF, Pt/C/NF, and NF at a scan rate of 5 mV s^{-1}. b) Tafel plots for the Ni_2P–NiP_2 HNPs/NF, Ni_2P HNPs/NF, NiP_2 HNPs/NF, C-Ni_2P/NF, and Pt/C/NF. c) The half of current density variation (j_{anodic} − $j_{cathodic}$) at 0.21 V versus RHE plotted against scan rate for the Ni_2P–NiP_2 HNPs/NF, Ni_2P HNPs/NF, NiP_2 HNPs/NF, and C-Ni_2P/NF. d) Nyquist plots of the Ni_2P–NiP_2 HNPs/NF, Ni_2P HNPs/NF, NiP_2 HNPs/NF measured at an overpotential of 100 mV. They have the same equivalent circuit as inserted in panel (d). e) Polarization curves of the Ni_2P–NiP_2 HNPs/NF at initial and after 1000 CV cycles from −600 to 60 mV versus RHE at 50 mV s^{-1}. f) Chronoamperometric curve of the Ni_2P–NiP_2 HNPs/NF recorded at 85 mV versus RHE for 24 h.

Figure S9 (Supporting Information). For the initial sample and sample after long-term HER tests, the peaks at 854.5 eV could be ascribed to Ni 2p$_{3/2}$ in Ni_2P–NiP_2 HNPs, which are between Ni 2p$_{3/2}$ of Ni_2P (853.2 eV)[37] and that of NiP_2 (856.6 eV).[38] The mid-value might result from the electron transfer from Ni atom to P atom at the heterointerface of Ni_2P and NiP_2,[15] which was later confirmed by DFT calculation. The peaks at ≈856 eV could be indexed to Ni 2p$_{3/2}$ in oxidized Ni species arising from superficial oxidation of the Ni_2P–NiP_2 HNPs which once exposed in air.[39] The other peaks at ≈860 eV can be assigned to the satellites of Ni 2p$_{3/2}$ peaks.[40] The peaks at ≈129 and ≈130 eV in the P 2p spectra can be indexed to P 2p$_{3/2}$ and P 2p$_{1/2}$ in Ni_2P–NiP_2 HNPs, respectively.[41] The other peaks at ≈133 eV can be assigned to phosphate (PO$_x$) signals.[39] By comparison, it could deduce that there is no obvious compositional change, except the oxidation degree increasing after 1000 LSV scanning.

It might ascribed to more contact between electrodes and the electrolyte (OH$^-$ or H_2O), causing the increase of relative Ni–O and P–O peak areas. Furthermore, in situ Raman spectra of the Ni_2P–NiP_2 HNPs/NF electrodes before and after HER conditions (Figure S10, Supporting Information) detect no Raman peaks of Ni(OH)$_x$ or NiO,[42,43] suggesting no remarkable signal changes. That is, the trace amount of superficial oxidation of the Ni_2P–NiP_2 HNPs has no obvious influence on their HER performance.

For designing a well matched electrode pair with low cell voltage for overall water splitting, Ni-Fe LDH compound with outstanding catalytic activity was chosen as OER catalyst. The as-prepared NiFe-LDH nanosheet arrays grown on nickel foam (NiFe-LDH/NF) were confirmed to be $Ni_6Fe_2(CO_3)(OH)_{16}\cdot4H_2O$ sheets with a thick of ≈25 nm (Figure S11, Supporting Information). **Figure 3**a shows the NiFe-LDH with hydrotalcite-like
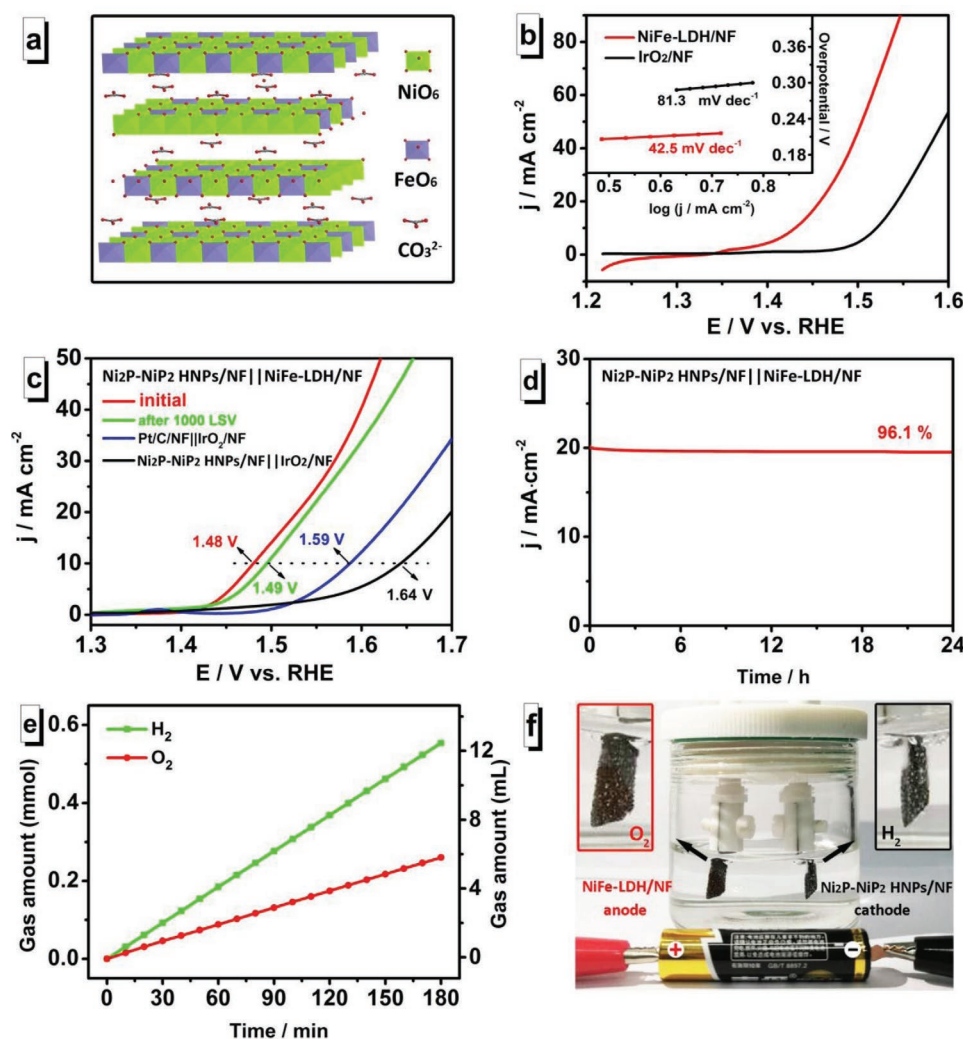
Figure 3. a) Atomic structure of the NiFe-LDH with interlayer carbonate anions. b) Polarization curves for the OER in 1 M KOH using the NiFe-LDH/NF and the commercial IrO_2 catalyst/NF (IrO_2/NF), with corresponding Tafel plots inserted. c) Polarization curves of Ni_2P–NiP_2 HNPs/NF‖NiFe-LDH/NF pair at initial and after 1000 LSV scanning in a two-electrode water-splitting system in 1 M KOH. The Pt/C/NF‖IrO_2/NF pair and Ni_2P–NiP_2 HNPs/NF‖IrO_2/NF pair were measured for comparison. d) Chronoamperometry of water electrolysis using the Ni_2P–NiP_2 HNPs/NF‖NiFe-LDH/NF as electrode pair at a voltage of 1.53 V in 1 M KOH for 24 h electrolysis. e) Experimentally measured O_2 and H_2 amounts by the drainage method. f) Demonstration of two-electrode water-splitting device powered by an AAA battery with a nominal voltage of 1.5 V.

structure is composed of edge sharing octahedral MO_6 layers and interlayer carbonate anions. As proven by other scientists, carbonate insertion will promote the catalytic performance of the NiFe-LDH.[44] The OER properties of the as-synthesized NiFe-LDH were evaluated using a typical three-electrode system under 1 M KOH. The commercial IrO_2 was measured for comparison. Figure 3b shows the polarization curves with a corresponding Tafel plots inserted. The NiFe-LDH/NF only requires overpotential of 200 mV to reach 10 mA cm^{-2}, even lower than that of the commercial IrO_2/NF (IrO_2/NF) (289 mV). The Tafel slope for the NiFe-LDH/NF is 42.5 mV dec^{-1}, also smaller than that of the IrO_2 /NF (81.3 mV dec^{-1}), which indicates that the NiFe-LDH/NF had smaller charge transfer resistance.[45] As shown in Figure 3c, a combined electrode pair could deliver overall water splitting with a current density of 10 mA cm^{-2} at a voltage of 1.48 V (with 20 mA cm^{-2} at 1.53 V) using the

Ni_2P–NiP_2 HNPs/NF as cathode and the NiFe-LDH/NF as anode, corresponding to a low overpotential of 250 mV. For comparison, the typical Pt/C/NF‖IrO_2/NF couple requires 1.59 V to reach a current density of 10 mA cm^{-2}, corresponding to the overpotential of 360 mV, and the Ni_2P–NiP_2 HNPs/NF‖IrO_2/NF couple requires 1.64 V to reach a current density of 10 mA cm^{-2}, corresponding to the overpotential of 410 mV. The stability of the Ni_2P–NiP_2 HNPs/NF‖NiFe-LDH/NF couple was checked by taking continuous linear sweep voltammetry at an accelerated scanning rate of 20 mV s^{-1} till 1000 cycles. As shown in Figure 3c, the overpotential for achieving 10 mA cm^{-2} only increases 10 mV after 1000 cycles. Moreover, the long-term electrochemical stability of this electrolyzer was carried out at a potential of 1.53 V. As shown in Figure 3d, the Ni_2P–NiP_2 HNPs/NF‖Ni-Fe LDH/NF couple possesses an initial current density of 20 mA cm^{-2}, which could maintain 96.1% retention
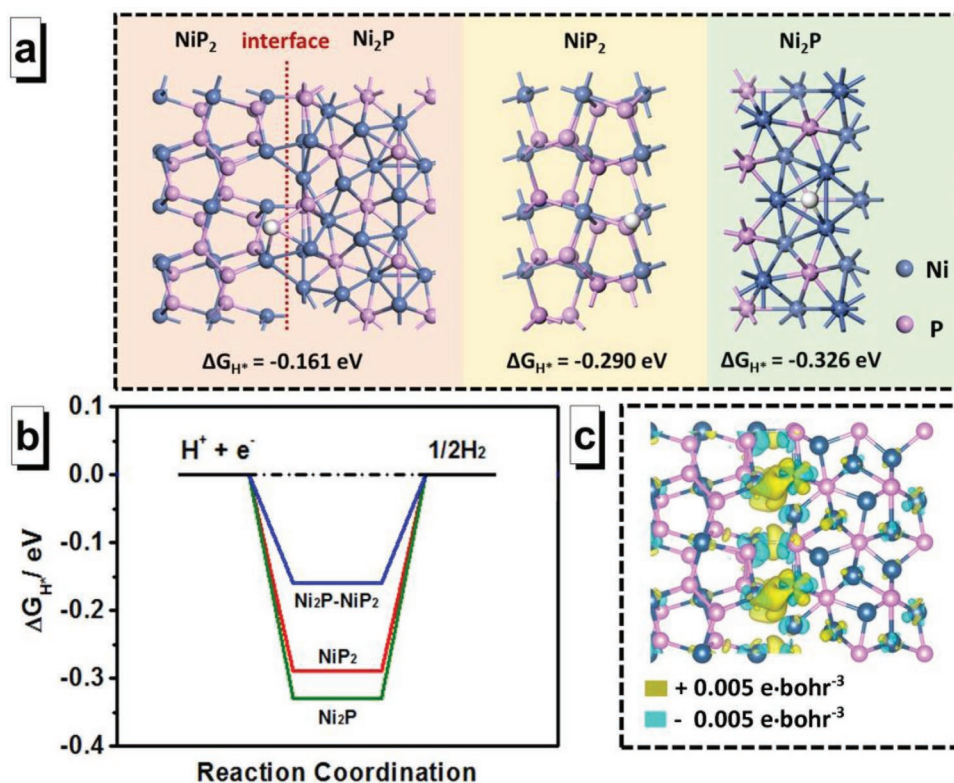
Figure 4. a) Top view of the schematic models of the optimized Ni_2P–NiP_2 polymorph, and pure NiP_2 as well as Ni_2P with H* adsorbed on their surfaces. b) HER free-energy diagram calculated at the equilibrium potential for the Ni_2P–NiP_2 polymorph, pure NiP_2, and pure Ni_2P. c) Charge density difference plot at the Ni_2P–NiP_2 interface.

after 24 h. The H_2 and O_2 gases produced at 10 mA cm^{-2} were quantitatively collected by the drainage method. As shown in Figure 3e, the measured H_2 and O_2 amount shows a molar ratio close to 2:1, according to the volume-time curve of the collected H_2 and O_2. We calculate and obtain the faradic efficiencies of Ni_2P–NiP_2 HNPs/NF and NiFe-LDH/NF as ≈99% and ≈93%, respectively. Excitingly, our water-splitting device could be driven by a single-cell AAA battery with a nominal voltage of ≈1.5 V at room temperature, as demonstrated in Figure 3f and Movie S1 (Supporting Information) of water electrolysis. To the best of our knowledge, we assembled the asymmetric water electrolyzer of the Ni_2P–NiP_2 HNPs/NF||Ni-Fe LDH/NF, which is superior to some bifunctional nickel phosphides electrolyzers and NiFe-LDH electrolyzers, such as the Co_4NiP nanotubes||Co_4NiP nanotubes (1.59 V),[30] the multishelled Ni_2P||multishelled Ni_2P (1.57 V),[31] the $(Ni_{0.33}Fe_{0.67})_2P$ ||$(Ni_{0.33}Fe_{0.67})_2P$ (1.54 V),[46] the Cu nanowires@NiFe-LDH||Cu nanowires@NiFe-LDH (1.54 V)[47] and NiFeRu-LDH||NiFeRu-LDH (1.52 V).[48] Furthermore, it is also better than some asymmetric water electrolyzers, such as the NiFe-P||NiFeO$_x$ (1.7 V for 20 mA cm^{-2}),[49] the CoNi(OH)$_x$||NiN$_x$ (1.65 V)[50] and other couples (Table S2, Supporting Information).

It is well known that a catalyst that gives $\Delta G_{H*} = 0$ is served as an ideal candidate for HER. The lower absolute values of ΔG_{H*} enables a preferable H* adsorption strength.[19–22] In order to better understand heterointerface effect on enhanced HER activity, the DFT calculations were performed to estimate the ΔG_{H*} of heterojunction of Ni_2P–NiP_2, pure NiP_2 and Ni_2P

models. According to the finite strain theory, we fabricated the most matched interface of $(100)_{Ni2P}$-$(100)_{NiP2}$, with an interfacial strain of ≈5%. Figure 4a exhibits the schematic models of Ni_2P–NiP_2 heterostructure, pure-phased NiP_2 and pure-phased Ni_2P, where H* adsorbed on P site, P site and trigonal Ni_3 site, respectively. The ΔG_{H*} values of Ni_2P–NiP_2, pure-phased NiP_2 and pure-phased Ni_2P are described in Figure 4b. The ΔG_{H*} of Ni_2P–NiP_2 (P site) is −0.161 eV, which is superior than that of Ni_2P (trigonal Ni_3 site) (−0.326 eV) and NiP_2 (P) (−0.290 eV) for HER. This result could be explained by calculating the different charge densities at the same adsorption sites. As shown in Figure 4c, we observe that the strong charge redistribution occurred at the interface region. According to Bader charge analysis, the average valance charge for P (NiP_2) site near the Ni_2P–NiP_2 interface change from 5.22 eV to 5.05 eV, which could be helpful for hydrogen desorption from P site (Ni_2P–NiP_2), and avoid the catalysts poisoning.[15] From the analysis above, we discussed that the P sites near Ni_2P–NiP_2 interfaces served as the actual active sites for HER. And heterointerface effect could optimize the valence electron state of active sites and enhance the electronic conductivity of catalyst, therefore, the Ni_2P–NiP_2 polymorph exhibits superior HER performance.

In summary, hollow Ni_2P–NiP_2 polymorph with ≈100 nm in diameter and ≈6 nm in thickness has been synthesized using single-crystal NiS_2 octahedrons as sacrificial template based on nanoscaled Kirkendall effect. It only requires an overpotential of 59.7 mV to achieve 10 mA cm^{-2} with a Tafel slope of 58.8 mV dec^{-1}, comparable to Pt/C (requiring 41.5 mV and

Tafel slope of 40.5 mV dec^{-1}), superior to Ni$_2$P hollow nanoparticles (requiring 104.8 mV and Tafel slope of 85.3 mV dec^{-1}), NiP$_2$ hollow nanoparticles (requiring 82.2 mV and Tafel slope of 70.3 mV dec^{-1}), and commercial solid Ni$_2$P NPs (requiring 130.8 mV and Tafel slope of 87.7 mV dec^{-1}). According to DFT calculation results, we demonstrate that electrons transfer from P to Ni at the heterointerfaces, which decreases the absolute value of H* adsorption energy and simultaneously enhance electronic conductivity. And such a hollow structure with high specific area could fully show the advantage of heterostructure. Furthermore, we exemplified the high-performance of the Ni$_2$P–NiP$_2$ polymorph to fabricate an two-electrode alkaline electrolyzer combined with a NiFe-LDH electrode, which could reach 10 mA cm^{-2} in 1 M KOH at 1.48 V (with a ultra-low overpotential of 250 mV), and remain a current density of 96.1% after 24 h electrolysis at 1.53 V. This electrolyzer also confirms to be driven by an AAA battery with a nominal voltage of 1.5 V. This work provides a feasible strategy to fabricate high-efficient polymorph electrocatalyst by forming metallic-metalloid composites to control interfacial charges.

Experimental Section

Synthesis of NiS$_2$ Octahedrons: For the synthesis of NiS$_2$ nanooctahedrons with an average size of 100 nm, 1 mmol of NiCl$_2$·6H$_2$O, 2.5 mmol of Na$_2$S$_2$O$_3$·5H$_2$O and 550 mg of PVP were dissolved in 35 mL of milli-Q water, and stirred for 30 min to form uniform transparent solution. Afterward, the solution was transferred into 50 mL Teflon-lined autoclave, hydrothermally treated at 150 °C for 12 h, and then cooled down to room temperature. The product was collected by centrifugation and washed several times with deionized water and subsequently dried in a freezer dryer for 24 h.[51]

Synthesis of Ni$_2$P–NiP$_2$ HNPs: The Ni$_2$P–NiP$_2$ HNPs were synthesized by a solid-state phosphorization reaction between NaH$_2$PO$_2$ and NiS$_2$ single-crystal octahedrons precursor. In a typical chemical transformation procedure, 20 mg of NiS$_2$ precursor was added into 8 mL of aqueous solution containing NaH$_2$PO$_2$ (400 mg). The uniform suspension was obtained by vigorous agitation and supersonic dispersion. The powder of mixture was obtained by freeze-drying. Next, the mixture was thoroughly mixed with a mortar and pestle, and treated at 350 °C in N$_2$ atmosphere for 10 h. The product was collected by centrifugation and washed several times with deionized water and ethanol.

Synthesis of Ni$_2$P HNPs: The process was the same as that used for the synthesis of the Ni$_2$P–NiP$_2$ HNPs except that the mixture was heat treated at 300 °C in N$_2$ atmosphere for 5 h.

Synthesis of NiP$_2$ HNPs: The process was the same as that used for the synthesis of the Ni$_2$P–NiP$_2$ HNPs except that the mixture was heat treated at 400 °C in N$_2$ atmosphere for 10 h.

Synthesis of NiFe-LDH: In a typical process, a piece of nickel foam (NF, 2 cm × 4 cm) was cleaned ultrasonically with 3 M HCl solution and the mixture of acetone, ethanol, and deionized (DI) water in sequence before use. Then, 0.75 mmol Ni(NO$_3$)$_2$·6H$_2$O, 0.25 mmol Fe(NO$_3$)$_3$·4H$_2$O, 3 mmol urea, and 3 mmol NH$_4$F were dispersed in 30 mL of milli-Q water, and stirred for 10 min to form uniform transparent solution. The obtained solution was then transferred into a 50 mL Teflon-lined autoclave. Subsequently, the cleaned nickel foam was placed into autoclave sealed and heated at 140 °C for 4 h in an oven, which was then cooled down to room temperature naturally. The resulting materials were rinsed with DI water and ethanol several times, and then dried at 60°C for further use.

Material Characterizations: The scanning electron microscopy images were captured using a Hitachi 7500 field-emission gun scanning electron microscope. The TEM and HRTEM were carried out by a JEOL JEM-2100F

at an acceleration voltage of 200 kV. The composition and structure of products were characterized by a Rigaku Dmax 2200 XRD with Cu K$_\alpha$ radiation ($\lambda = 1.5416$ Å). The XPS were collected on an ESCALAB 250 electron spectrometer from ThermoFisher Scientific Corporation with monochromatic 150 W Al K$_\alpha$ radiation. All the spectra were adjusted to the C 1s at Binding Energy of 284.8 eV. The concentration of Ni and P in the aqueous solution was analyzed via an ICP-OES (Agilent 710).

Electrochemical Measurements: All measurements were carried out with an electrochemical workstation (Gamry, Interface1000, USA). For the electrocatalytic HER in 1 M KOH, a 1 cm × 1 cm cleaned Ni foam uniformly coating by ≈5 mg sample was used as the work electrode after calcination under N$_2$ atmosphere at 350 °C for 3 h. The Ag/AgCl (3.3 mol L^{-1} KCl) electrode and the platinum wire were used as the reference and the counter electrode, respectively. LSV with a scan rate of 5 mV s^{-1} and CV cycling tests with a scan rate of 50 mV s^{-1} were conducted in the range of −600 to 60 mV versus RHE and chronoamperometry (CA) with 20 mA cm^{-2} for 24 h. The ECSA was estimated from the electrochemical double-layer capacitance (C_{dl}). The C_{dl} was determined with typical CV tests at various scan rates (5, 10, 20, 30, 40, 50 mV s^{-1}) in 0.16–0.26 V versus RHE region. The C_{dl} was estimated by plotting the half of the difference between anodic current density and cathodic current density ($j_a − j_c$) at 0.21 V versus RHE against the scan rate. For the electrocatalytic OER in 1 M KOH, the NiFe-LDH/NF slices were cut to the size of 1.0 cm × 1.0 cm as the working electrode. The Ag/AgCl (3.3 mol L^{-1} KCl) electrode and the platinum wire were used as reference and counter electrodes, respectively. LSV with a scan rate of 5 mV s^{-1} was conducted. In this work, the potentials were calculated versus the RHE by equation

$$E_{RHE} = E_{Ag/AgCl} + 0.197 + 0.0591 \times pH$$

where $E_{Ag/AgCl}$ is the measured potential referring to the Ag/AgCl reference electrode. For the overall water splitting, the Ni$_2$P–NiP$_2$ HNPs/NF and the Ni-Fe LDH/NF were used as cathode and anode to construct two-electrode system. LSV with a scan rate of 5 mV s^{-1} was conducted. The stability of the Ni$_2$P–NiP$_2$ HNPs/NF‖Ni-Fe LDH/NF couple was checked by taking continuous LSV at an accelerated scanning rate of 20 mV s^{-1} till 1000 cycles, and CA with 20 mA cm^{-2} for 24 h. For the hydrogen and oxygen production measurement, the H$_2$ and O$_2$ gases produced at 10 mA cm^{-2} were quantitatively collected by the drainage method. The faradic efficiency is calculated by equation

$$FE = \frac{m \times n \times F}{I \times t} \times 100\%$$

where m is the number of moles of produced hydrogen, n is the number of electrons transfer, F is the Faraday constant, I is current, and t is time.

In Situ Raman Spectroscopy: Raman spectroscopy was recorded on Renishaw inVia Reflex Raman microscope under an excitation of 532 nm laser light with power of 20 mW. The water electrolyzer was constructed by Teflon with thin round quartz glass plate as cover to protect the objective. The 0.5 cm × 0.5 cm working electrode was put on a columnar conducting electrode to keep the plane of working electrode perpendicular to the incident laser. A Pt wire as the counter electrode was rolled to a circle around the cell. The Ag/AgCl electrode with inner reference electrolyte of 3.3 mol L^{-1} KCl was used as the reference electrode.

Theoretical Section: Computation Details: The DFT computations were carried out using the Vienna ab initio simulation package (VASP v.5.4.1).[52,53] During all calculations, the generalized gradient approximation and the projector augments wave pseudopotentials with the exchange and correlation in the Perdew–Burke–Ernzerhof were employed.[54,55] The plane-wave cutoff energy is set at 400 eV. The convergence threshold is set as 10^{-5} eV in energy and 0.02 eV Å^{-1} in force, respectively. The DFT + U technique was applied to the Ni atom, where a value of 3.8 eV was used for the U–J parameter for Ni 3d states.[56] The spin polarization was setup to all the calculations. Dipole correction along the direction perpendicular to the surface was included for all slab calculations. The Monkhorst–Pack Gamma-centered k-points

mesh was adopted for all calculations, where the spacing of uniformly sampled k points for each simulation is set to be no larger than $2\pi \times 0.02$ Å^{-1}.

Theoretical Section: Theoretical Models: The unit cells of Ni_2P and NiP_2 were in the P-62m and PA-3 symmetry groups, respectively.[57] Crystallographic transformation was first performed to change the triclinic cell of Ni_2P into the orthorhombic cell. Then, the heterogeneous interface model was built by (1×3) Ni_2P (100) and (1×2) NiP_2 (100) with an small interfacial strain of ≈5%. For computing the hydrogen adsorption energy, layer slab models of pure Ni_2P, pure NiP_2, and Ni_2P/NiP_2 heterojunction were constructed, respectively, with a vacuum layer of 20 Å. For geometry optimizations of all slab models, the top two layers were allowed to relax. The free energy of hydrogen adsorption on (001) surface of Ni_2P, (001) surface of NiP_2, and Ni_2P/NiP_2 hybrid nanostructure were calculated using the equation $\Delta G_H = E_{ads} + \Delta E_{ZPE} - T\Delta S_H$, where the ΔE_{ZPE} is the change in zero-point energy of surface vibrations upon hydrogen adsorption, and ΔS_H is the entropy of adsorption, approximated by half the entropy of molecular hydrogen in gas phase. Therefore, the free energy of the adsorbed state can be taken as $\Delta G_H = \Delta E_{H^*} + 0.24$ eV.[58]

Supporting Information

Supporting Information is available from the Wiley Online Library or from the author.

Acknowledgements

Conflict of Interest

The authors declare no conflict of interest.

Keywords

[1] M. S. Dresselhaus, I. L. Thomas, *Nature* **2001**, *414*, 332.
[2] A. Manabe, M. Kashiwase, T. Hashimoto, T. Hayashida, A. Kato, K. Hirao, I. Shimomura, I. Nagashima, *Electrochim. Acta* **2013**, *100*, 249.
[3] K. Zeng, D. Zhang, *Prog. Energy Combust. Sci.* **2010**, *36*, 307.
[4] Y. Ge, P. Dong, S. R. Craig, P. M. Ajayan, M. Ye, J. Shem, *Adv. Energy Mater.* **2018**, *8*, 1800484.
[5] Y. Pan, K. Sun, S. Liu, X. Cao, K. Wu, W.-C. Cheong, Z. Chen, Y. Wang, Y. Li, Y. Liu, D. Wang, Q. Peng, C. Chen, Y. Li, *J. Am. Chem. Soc.* **2018**, *140*, 2610.
[6] Y. Li, H. Zhang, M. Jiang, Q. Zhang, P. He, X. Sun, *Adv. Funct. Mater.* **2017**, *27*, 1702513.
[7] H. Li, Q. Li, P. Wen, T. B. Williams, S. Adhikari, C. Dun, C. Lu, D. Itanze, L. Jiang, D. L. Carroll, G. L. Donati, P. M. Lundin, Y. Qiu, S. M. Geyer, *Adv. Mater.* **2018**, *30*, 1705796.
[8] M.-Q. Wang, C. Ye, H. Liu, M. Xu, S.-J. Bao, *Angew. Chem., Int. Edi.* **2018**, *57*, 1963.
[9] Y. Wang, B. Kong, D. Zhao, H. Wang, C. Selomulya, *Nano Today* **2017**, *15*, 26.
[10] Z. Jin, P. Li, D. Xiao, *Green Chem.* **2016**, *18*, 1459.
[11] J. F. Callejas, C. G. Read, E. J. Popczun, J. M. McEnaney, R. E. Schaak, *Chem. Mater.* **2015**, *27*, 3769.
[12] J. Song, C. Zhu, B. Z. Xu, S. Fu, M. H. Engelhard, R. Ye, D. Du, S. P. Beckman, Y. Lin, *Adv. Energy Mater.* **2017**, *7*, 1601555.
[13] A. Wu, Y. Xie, H. Ma, C. Tian, Y. Gu, H. Yan, X. Zhang, G. Yang, H. Fu, *Nano Energy* **2018**, *44*, 353.
[14] I. S. Amiinu, Z. Pu, X. Liu, K. A. Owusu, H. G. R. Monestel, F. O. Boay, H. Zhang, S. Mu, *Adv. Funct. Mater.* **2017**, *27*, 1702300.
[15] K. Wang, X. She, S. Chen, H. Liu, D. Li, Y. Wang, H. Zhang, D. Yang, X. Yao, *J. Mater. Chem. A* **2018**, *6*, 5560.
[16] Y. Liu, G. Yu, G.-D. Li, Y. Sun, T. Asefa, W. Chen, X. Zou, *Angew. Chem., Int. Edi.* **2015**, *54*, 10752.
[17] C. Zhu, A.-L. Wang, W. Xiao, D. Chao, X. Zhang, N. H. Tiep, S. Chen, J. Kang, X. Wang, J. Ding, J. Wang, H. Zhang, H. J. Fan, *Adv. Mater.* **2018**, *30*, 1705516.
[18] C. Guan, W. Xiao, H. Wu, X. Liu, W. Zang, H. Zhang, J. Ding, Y. P. Feng, S. J. Pennycook, J. Wang, *Nano Energy* **2018**, *48*, 73.
[19] H. Li, C. Tsai, A. L. Koh, L. Cai, A. W. Contryman, A. H. Fragapane, J. Zhao, H. S. Han, H. C. Manoharan, F. Abild-Pedersen, J. K. Nørskov, X. Zheng, *Nat. Mater.* **2016**, *15*, 48.
[20] T. Ling, D.-Y. Yan, H. Wang, Y. Jiao, Z. Hu, Y. Zheng, L. Zheng, J. Mao, H. Liu, X.-W. Du, M. Jaroniec, S.-Z. Qiao, *Nat. Commun.* **2017**, *8*, 1509.
[21] T. F. Jaramillo, K. P. Jørgensen, J. Bonde, J. H. Nielsen, S. Horch, I. Chorkendorff, *Science* **2007**, *317*, 100.
[22] P. Xiao, W. Chen, X. Wang, *Adv. Energy Mater.* **2015**, *5*, 1500985.
[23] M. Gong, W. Zhou, M.-C. Tsai, J. Zhou, M. Guan, M.-C. Lin, B. Zhang, Y. Hu, D.-Y. Wang, J. Yang, S. J. Pennycook, B.-J. Hwang, H. Dai, *Nat. Commun.* **2014**, *5*, 4695.
[24] X.-Y. Yu, Y. Feng, Y. Jeon, B. Guan, X. W. Lou, U. Paik, *Adv. Mater.* **2016**, *28*, 9006.
[25] W. Zhou, W. Chen, J. Nai, P. Yin, C. Chen, L. Guo, *Adv. Funct. Mater.* **2010**, *20*, 3678.
[26] J. S. Cho, Y. J. Hong, Y. C. Kang, *ACS Nano* **2015**, *9*, 4026.
[27] J. Yu, Q. Li, Y. Li, C.-Y. Xu, L. Zhen, V. P. Dravid, J. Wu, *Adv. Funct. Mater.* **2016**, *26*, 7644.
[28] G. Anandhababu, Y. Huang, D. D. Babu, M. Xu, Y. Wang, *Adv. Funct. Mater.* **2018**, *28*, 1706120.
[29] G.-F. Chen, T. Y. Ma, Z.-Q. Liu, N. Li, Y.-Z. Su, K. Davey, S.-Z. Qiao, *Adv. Funct. Mater.* **2016**, *26*, 3314.
[30] L. Yan, L. Cao, P. Dai, X. Gu, D. Liu, L. Li, Y. Wang, X. Zhao, *Adv. Funct. Mater.* **2017**, *27*, 1703455.
[31] H. Sun, X. Xu, Z. Yan, X. Chen, F. Cheng, P. S. Weiss, J. Chen, *Chem. Mater.* **2017**, *29*, 8539.
[32] H. Jin, J. Wang, D. Su, Z. Wei, Z. Pang, Y. Wang, *J. Am. Chem. Soc.* **2015**, *137*, 2688.
[33] Y. Li, H. Wang, L. Xie, Y. Liang, G. Hong, H. Dai, *J. Am. Chem. Soc.* **2011**, *133*, 7296.
[34] Y. Liu, Q. Li, R. Si, G. D. Li, W. Li, D. P. Liu, D. Wang, L. Sun, Y. Zhang, X. Zou, *Adv. Mater.* **2017**, *29*, 1606200.
[35] Y.-Y. Chen, Y. Zhang, X. Zhang, T. Tang, H. Luo, S. Niu, Z.-H. Dai, L. J. Wan, J.-S. Hu, *Adv. Mater.* **2017**, *29*, 1703311.
[36] H. Liang, A. N. G, i, D. H. Anjum , X. Wang, U. Schwingenschlogl, H. N. Alshareef, *Nano Lett.* **2016**, *16*, 7718.
[37] J. Li, M. Yan, X. Zhou, Z.-Q. Huang, Z. Xia, C.-R. Chang, Y. Ma, Y. Qu, *Adv. Funct. Mater.* **2016**, *26*, 6785.

[38] Z. Pu, Y. Xue, W. Li, I. S. Amiinu, S. Mu, *New J. Chem.* **2017**, *41*, 2154.

[39] C. Du, M. Shang, J. Mao, W. Song, *J. Mater. Chem. A* **2017**, *5*, 15940.

[40] J. Zheng, W. Zhou, T. Liu, S. Liu, C. Wang, L. Guo, *Nanoscale* **2017**, *9*, 4409.

[41] X. Wang, R. Tong, Y. Wang, H. Tao, Z. Zhang, H. Wang, *ACS Appl. Mater. Interfaces* **2016**, *8*, 34270.

[42] N. Mironova-Ulmane, A. Kuzmin, I. Steins, J. Grabis, I. Sildos, M. Paers, *J. Phys.: Conf. Ser.* **2007**, *93*, 012039.

[43] O. Diaz-Morales, D. Ferrus-Suspedra, M. T. M. Koper, *Chem. Sci.* **2016**, *7*, 2639.

[44] B. M. Hunter, W. Hieringer, J. R. Winkler, H. B. Gray, A. M. Müller, *Energy Environ. Sci.* **2016**, *9*, 1734.

[45] Y. Jia, L. Zhang, G. Gao, H. Chen, B. Wang, J. Zhou, M. T. Soo, M. Hong, X. Yan, G. Qian, J. Zou, A. Du, X. Yao, *Adv. Mater.* **2017**, *29*, 1700017.

[46] Y. Li, H. Zhang, M. Jiang, Q. Zhang, Y. He, X. Sun, *Adv. Funct. Mater.* **2017**, *27*, 1702515.

[47] L. Yu, H. Zhou, J. Sun, F. Qin, F. Yu, J. Bao, Y. Yu, S. Chen, Z. Ren, *Energy Environ. Sci.* **2017**, *10*, 1820.

[48] G. Chen, T. Wang, J. Zhang, P. Liu, H. Sun, X. Zhuang, M. Chen, X. Feng, *Adv. Mater.* **2018**, *30*, 1706279.

[49] J. Wang, L. Ji, S. Zuo, Z. Chen, *Adv. Energy Mater.* **2017**, *7*, 1700107.

[50] S. Li, Y. Wang, S. Peng, L. Zhang, A. M. Al-Enizi, H. Zhang, X. Sun, G. Zheng, *Adv. Energy Mater.* **2016**, *6*, 1501661.

[51] J. Zheng, W. Zhou, Y. Ma, W. Cao, C. Wang, L. Guo, *Chem. Commun.* **2015**, *51*, 12863.

[52] G. Kresse, J. Hafner, *Phys. Rev. B* **1993**, *47*, 558.

[53] G. Kresse, J. Hafner, *Phys. Rev. B* **1994**, *49*, 14251.

[54] G. Kresse, J. Furthmüller, *Phys. Rev. B* **1996**, *54*, 11169.

[55] G. Kresse, D. Joubert, *Phys. Rev. B* **1999**, *59*, 1758.

[56] P. Li, X. Duan, Y. Kuang, Y. Li, G. Zhang, W. Liu, X. Sun, *Adv. Energy Mater.* **2018**, *8*, 1703341.

[57] E. Larsson, *Ark. Kem.* **1965**, *23*, 335.

[58] P. Wang, X. Zhang, J. Zhang, S. Wan, S. Guo, G. Lu, J. Yao, X. Huang, *Nat. Commun.* **2017**, *8*, 14580.